Nanoelectronics and Its New Materials – A NEW ERA OF NANOSCIENCE

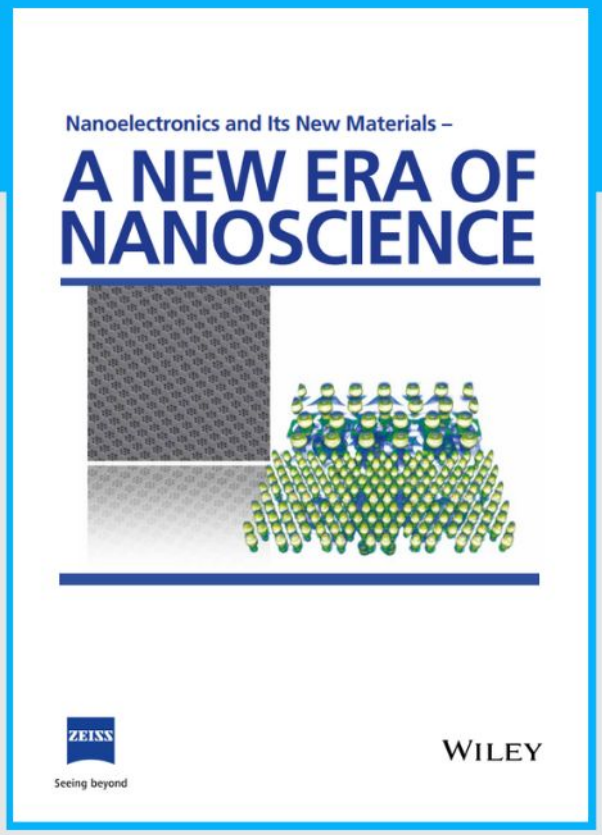

Discover the recent advances in electronics research and fundamental nanoscience.

Nanotechnology has become the driving force behind breakthroughs in engineering, materials science, physics, chemistry, and biological sciences. In this compendium, we delve into a wide range of novel applications that highlight recent advances in electronics research and fundamental nanoscience. From surface analysis and defect detection to tailored optical functionality and transparent nanowire electrodes, this eBook covers key topics that will revolutionize the future of electronics.

To get your hands on this valuable resource and unleash the power of nanotechnology, simply download the eBook now. Stay ahead of the curve and embrace the future of electronics with nanoscience as your guide.

ZEISS

Seeing beyond

WILEY

ADVANCED FUNCTIONAL MATERIALS
www.afm-journal.de

A Generic Sacrificial Layer for Wide-Range Freestanding Oxides with Modulated Magnetic Anisotropy

Huining Peng, Nianpeng Lu, Shuzhen Yang, Yingjie Lyu, Zhiwei Liu, Yifan Bu, Shengchun Shen, Mingqiang Li, Zhuolu Li, Lei Gao, Sicheng Lu, Meng Wang, Hui Cao, Hua Zhou, Peng Gao, Hanghui Chen, and Pu Yu**

Freestanding oxide nanomembranes have promising applications because of their novel electronic states and flexible crystalline structures. Several materials have been developed as sacrificial layers to exfoliate thin films from substrates via wet-etching. However, these materials face great challenges in terms of either complicated crystalline structures or corrosive solutions. Here, a new sacrificial material, $SrCoO_{2.5}$, is presented, which can be coherently grown with wide-range strains and crystalline orientations and is also soluble in eco-friendly solutions such as acetic acid, vinegar, and even carbonated drinks. With $SrCoO_{2.5}$ as the sacrificial layer, high-quality freestanding ferromagnetic $SrRuO_3$ membranes are achieved from wide-range epitaxial strains and different crystalline orientations. By investigating the evolution of the magnetic properties of these samples, it is discovered that epitaxial strain causes a distinct modification of the magnetic anisotropy of $(001)_{pc}$-oriented $SrRuO_3$ samples, while its influence on the $(110)_{pc}$ and $(111)_{pc}$ samples is insignificant. This study not only demonstrates the freestanding $SrRuO_3$ as a promising material for flexible spintronic devices, but also offers a great opportunity to engineer a wide range of strained and oriented complex oxides for novel freestanding electronics using this newly developed sacrificial material.

1. Introduction

Freestanding nanomembranes of complex oxides, which combine the scientific merits of correlated electronic states and structural flexibility, have attracted significant attention for both fundamental research and potential applications.[1–8] By removing the growth substrates and the corresponding clamping effects, freestanding membranes not only provide an exciting opportunity to probe stretching-induced novel electronic states,[8] but also offer an ideal platform to investigate epitaxial-strain-related electronic and magnetic states.[5] For instance, magnetic anisotropy in ferromagnetic complex oxides was revealed to be strongly correlated with epitaxial strain through the modification of oxygen octahedral rotations;[9–11] therefore, freestanding membranes offer an excellent platform to manipulate the magnetic properties of complex oxides.

H. Peng, S. Yang, Y. Lyu, S. Shen, Z. Li, S. Lu, M. Wang, P. Yu
State Key Laboratory of Low Dimensional Quantum Physics and Department of Physics
Tsinghua University
Beijing 100084, P. R. China
E-mail: yupu@mail.tsinghua.edu.cn

N. Lu, L. Gao
Beijing National Laboratory for Condensed Matter Physics
Institute of Physics
Chinese Academy of Sciences
Beijing 100190, P. R. China
E-mail: lunianpeng@iphy.ac.cn

N. Lu
Songshan Lake Materials Laboratory
Guangdong 523808, P. R. China

Z. Liu, Y. Bu, H. Chen
NYU-ECNU Institute of Physics
NYU Shanghai
Shanghai 200122, P. R. China

Z. Liu
Key Laboratory of Polar Materials and Devices (MOE) and Department of Electronics
East China Normal University
Shanghai 200241, P. R. China

M. Li, P. Gao
Electron Microscopy Laboratory
and International Center for Quantum Materials
School of Physics
Peking University
Beijing 100871, P. R. China

H. Cao
Materials Science Division
Argonne National Laboratory
Lemont, IL 60439, USA

H. Zhou
Advanced Photon Source
Argonne National Laboratory
Lemont, IL 60439, USA

P. Gao
Collaborative Innovation Centre of Quantum Matter
Beijing 100871, P. R. China

The ORCID identification number(s) for the author(s) of this article can be found under https://doi.org/10.1002/adfm.202111907.

DOI: 10.1002/adfm.202111907

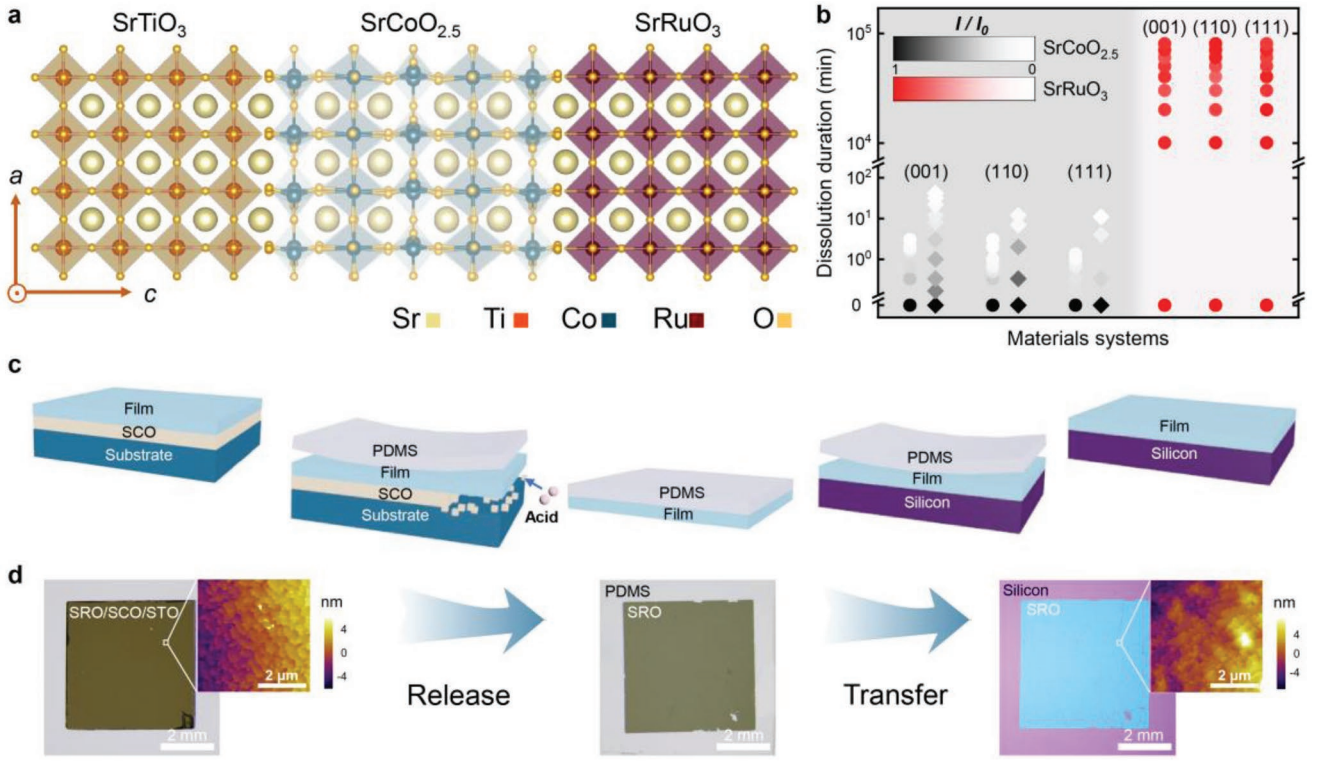

Figure 1. Design and fabrication of freestanding $SrRuO_3$ nanomembranes. a) Schematic illustration of an $SrRuO_3/SrCoO_{2.5}$ heterostructure grown on an $SrTiO_3$ (STO, (001)) substrate. b) Solubility tests for $SrCoO_{2.5}$ (SCO, black) and $SrRuO_3$ (SRO, red) thin films (30 nm) immersed in vinegar (circle) and a carbonated drink (diamond), respectively, where *I* represent the intensity of the characteristic XRD peaks extracted from time-dependent XRD 2θ-ω scans (Figure S1 and S2, Supporting Information). c) Schematic illustration of the exfoliation and transfer processes with SCO as the sacrificial layer. d) Optical images of a 30-nm-thick SRO thin film grown on SCO (30 nm)/STO (001) transferred to a PDMS support and then to an SiO_2/Si substrate. The insets show the surface morphology of SRO before and after exfoliation, where atomically smooth terraces are clearly identified.

The key to obtaining high-quality freestanding oxide membranes is the selection of a suitable sacrificial layer between the thin film and substrate and an appropriate solution to dissolve the sacrificial layer. Over the past decades, conventional complex oxides, such as $SrTiO_3$, MgO, and $La_{0.7}Sr_{0.3}MnO_3$, have been widely explored as sacrificial layers, which can be etched away by hydrofluoric acid or hydrochloric acid.[12–14] However, the high corrosiveness of these solutions is also deleterious to freestanding membranes. Recently, a promising water-soluble sacrificial material, $Sr_3Al_2O_6$ (SAO), was developed[5] and triggered a wide range of research interests.[6–8,15–17] However, the instability of SAO thin films in an atmospheric environment, owing to their water solubility, inevitably limits their practical applications.[18] Moreover, the complex crystalline structure of SAO increases growth difficulty and restricts film quality when it is adapting to large epitaxial strains and various crystalline orientations,[19,20] which is essential for complex oxide thin films to stabilize metastable phases and novel electronic states.[11,21] Bi-layer graphene has also been successfully developed to obtain freestanding oxide membranes[22]; however, it also faces the challenge of fabricating high-quality epitaxial thin films. Considering these facts and the rapid development of complex oxide freestanding membranes, it is highly desirable to explore alternative sacrificial layers to meet the tunability of wide-range epitaxial strains and various crystalline orientations, as well as to achieve moderate solubility in eco-friendly solutions.

In this study, brownmillerite $SrCoO_{2.5}$ (SCO) was successfully demonstrated as a promising sacrificial layer for obtaining high-quality freestanding oxide membranes from wide-range strained states and crystalline orientations. Bulk SCO has an orthorhombic structure with a pseudo-cubic lattice (a_{pc} = 3.905 Å and c_{pc} = 3.9363 Å), which can be epitaxially grown on a large collection of perovskites and related oxides.[23,24] More importantly, SCO is highly soluble in eco-friendly weak acid solutions, such as acetic acid, vinegar, and even carbonated drinks (see Video S1, Supporting Information). These features suggest SCO as a promising sacrificial material for obtaining high-quality complex oxide nanomembranes. We focused on ferromagnetic metallic $SrRuO_3$ (SRO) as a freestanding material in this study (**Figure 1**a), the structurally correlated magnetic anisotropy[11,21,25–27] and strong intrinsic spin-orbit coupling[28] of which ensure scientific interest and the technical importance of exploring its nanomembranes.

In this paper, we report the design of high-quality freestanding SRO nanomembranes with brownmillerite SCO as

H. Chen
Department of Physics
New York University
New York NY 10003, USA
P. Yu
Frontier Science Center for Quantum Information
Beijing 100084, P. R. China

the sacrificial layer. Because of the closely matched lattice structure of SCO with perovskites, as well as its high solubility in eco-friendly solutions, freestanding SRO nanomembranes were successfully exfoliated from various epitaxial substrates and crystalline orientations and then transferred onto flexible polydimethylsiloxane (PDMS) and silicon wafers. Importantly, freestanding SRO $(001)_{pc}$ nanomembranes exhibited remarkably modified magnetic anisotropy through strain relaxation while maintaining good metallicity. In contrast, the $(110)_{pc}$- and $(111)_{pc}$-oriented nanomembranes exhibited insignificant changes in magnetic anisotropy after exfoliation. This study not only sheds new light on the evolution of the magnetic states of SRO but also identifies SCO as a promising sacrificial layer to build a foundation for exploring a wide spectrum of novel complex oxide membranes.

2. Results

2.1. Design Principle and Fabrication of SRO Freestanding Nanomembranes

We first tested the solubility of SCO and SRO by soaking them in eco-friendly weak acid solutions (for example, vinegar and carbonated drinks) for a certain period. We performed ex situ X-ray diffraction (XRD) 2θ-ω scans on these thin films (Figures S1 and S2, Supporting Information), and the intensity of the characteristic diffraction peaks was used as an indicator of solubility (Figure 1b). The measurements clearly revealed that SCO dissolved in a few minutes with gradually disappearing XRD peaks, whereas SRO remained intact even after 8 weeks, as evidenced by its robust XRD peaks and well-preserved thickness fringes. The distinctive solubility of SCO compared with SRO, as well as the excellent stability of SCO under ambient conditions (Figure S3, Supporting Information), suggest that SCO can act as an ideal sacrificial layer to build freestanding oxide membranes.

We attributed the high reaction activity of SCO within weak acids to the unique crystalline structure of the oxygen vacancy channels. In SCO, although the octahedral and tetrahedral layers possess distinct crystal coordination, the Co ions share the same chemical valence state as Co^{3+}. This suggests a pronounced charge transfer between the octahedral and tetrahedral layers; consequently, the Co ions at the tetrahedral layers favor ionic bonding with the apical oxygen ions. We expect that such ionic bonds tend to react with hydrogen ions within the acids, leading to breakdown of the crystal structure.

To obtain high-quality freestanding SRO nanomembranes, SRO (30 nm) and SCO (30 nm) heterostructures were grown on STO (001) substrates using pulsed laser deposition (see Figure 1a and Experimental Section). The SRO/SCO/STO heterostructure was then covered with PDMS as a mechanical support layer and immersed in vinegar. After a few hours, the freestanding SRO membrane was successfully released from the substrate and electrostatically adsorbed onto PDMS. Finally, the intact membrane was transferred onto a silicon wafer or another substrate (Figure 1c). Note that the longer time as compared with the SCO only could be attributed to the fact that the dissolution process occurred mainly through the interface rather than pinholes and cracks across the SRO layer, which was essential for obtaining high-quality freestanding membranes. Consequently, we obtained a high-quality SRO nanomembrane, as shown in the optical images in Figure 1d. Note that the dimensions (≈0.5 cm × 0.5 cm) are mainly defined by the size of the substrates employed. Moreover, the atomically flat topographical surface (insets of Figure 1d) further highlights the integrity of the freestanding SRO nanomembranes after the transfer process.

2.2. Structural Evolution of SRO $(001)_{pc}$ Thin Films Before and After Exfoliation

Next, we investigated the structural evolution of SRO nanomembranes from their corresponding strained thin films. Besides the STO (001) substrate, with a compressive strain of −0.51%, we also employed LSAT (001) and DSO $(110)_o$ to impose a compressive strain of −1.45% and a tensile strain of 0.46% on SRO, respectively. As shown in **Figure 2**a, the systematic evolution of the SRO XRD (002) peaks was consistent with that of our previous studies on SRO directly grown on these substrates,[21] indicating excellent epitaxial growth, even with a buffered SCO layer. When the SCO thin film was grown on the DSO $(110)_o$ substrate, XRD superlattice peaks could not be detected, which was attributed to the tilted oxygen-vacancy channels from the film plane. Figure 2b shows the XRD scans of the corresponding SRO membranes, in which only the characteristic peaks from SRO were observed. Figure 2c summarizes the out-of-plane lattice parameter of both the strained and freestanding SRO samples. The lattice parameters of the as-grown samples demonstrated a good linear dependence on the epitaxial strain, verifying the excellent epitaxial nature of SRO thin films. All freestanding SRO membranes displayed a similar bulk-like lattice parameter (c_{pc} = 3.925 Å),[25] which clearly suggests that the epitaxial strain was completely relaxed through exfoliation.

Cross-sectional and plan-view high-angle annular dark-field transmission electron microscopy (HAADF-TEM) measurements were performed to characterize the crystalline quality of SRO before and after exfoliation. The sharp interfaces between SRO, SCO, and STO (Figure 2d; Figure S4a,d, Supporting Information) demonstrated that the as-grown heterostructure was coherently strained and free from any detectable interfacial dislocations and inter-diffusion. Atomically resolved cross-sectional (Figure 2e; Figure S4b,e, Supporting Information) and plan-view (Figure S4c, Supporting Information) HAADF images further demonstrated the high crystalline quality of the freestanding membranes. Furthermore, reciprocal space mapping (RSM) measurements were performed for both the as-grown SRO/SCO/STO heterostructures and freestanding SRO nanomembranes around the SRO $(103)_{pc}$ diffraction peak (Figure S5, Supporting Information), and the results were consistent with the XRD 2θ-ω scans and TEM results.

2.3. Strain-Dependent Magnetic Anisotropy

Noting that the magnetic anisotropy of SRO plays an essential role in its functionalities,[28] we investigated the evolution of

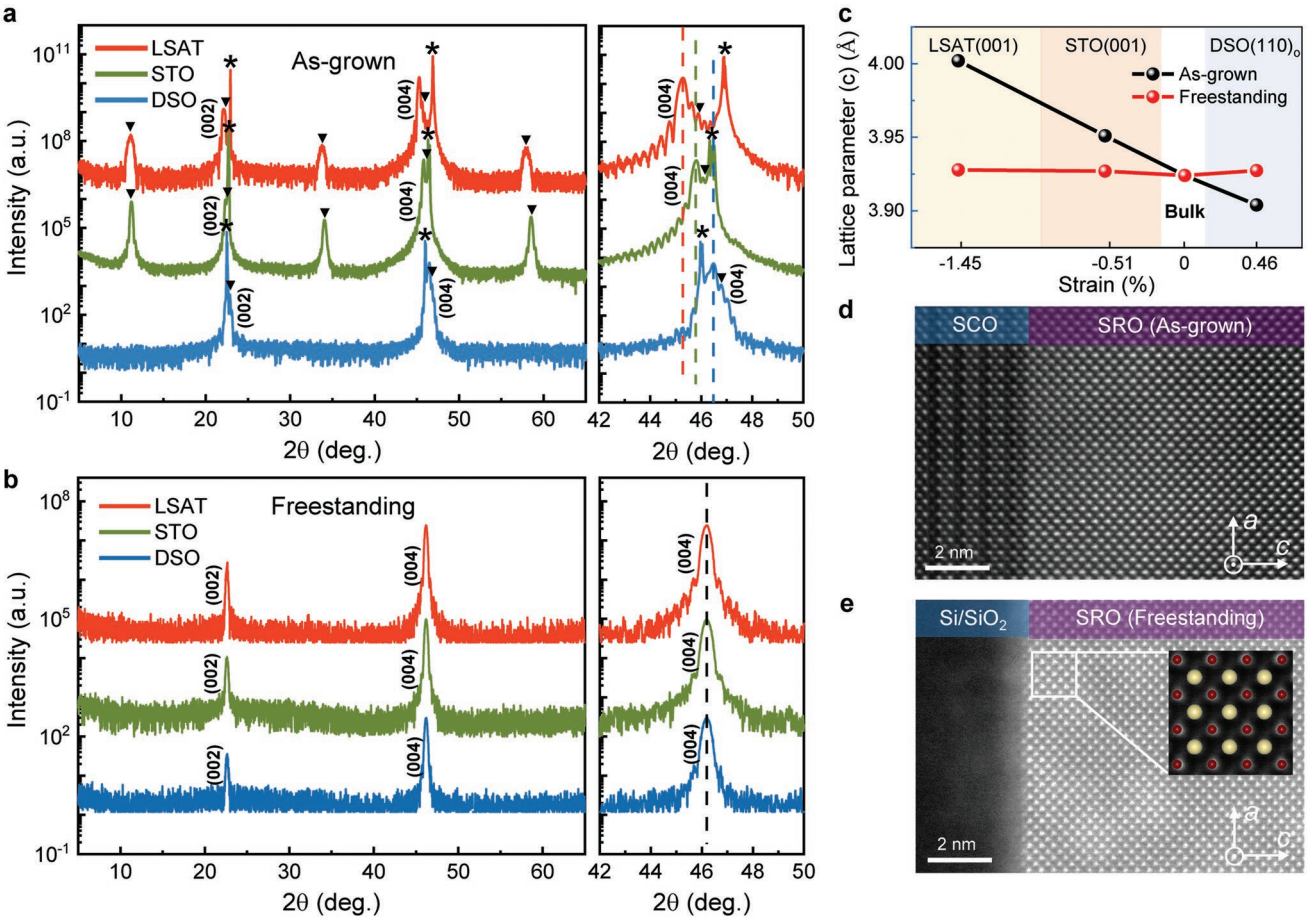

Figure 2. Crystal structure of strained SRO $(001)_{pc}$ thin films and corresponding freestanding nanomembranes. a,b) XRD 2θ-ω scans of a) as-grown SRO $(001)_{pc}$ thin films and b) the corresponding freestanding nanomembranes grown on LSAT (001) (red), STO (001) (green), and DSO $(110)_o$ (blue) substrates. Stars (*) and triangles (▼) indicate the diffraction peaks of the substrate and SCO, respectively. c) Summary of the out-of-plane lattice constant for SRO before and after exfoliation. d,e) Cross-sectional HAADF-TEM images of d) a typical as-grown SRO thin film on SCO/STO and e) the corresponding nanomembrane on an SiO_2/Si support. The inset in (e) shows a magnified crystalline structure for freestanding SRO, in which the red and yellow circles represent Ru and Sr atoms, respectively.

magnetic anisotropy between the as-grown and freestanding SRO thin films. Assuming that the magnetic moments at the remnant state point mainly toward its magnetic easy axis,[29] we estimated the magnetic anisotropy of our SRO samples by comparing the measured remnant magnetization along the out-of-plane (OOP) and in-plane (IP) directions (**Figure 3**a). Specifically, the angle (θ_{EA}) between the easy axis and the sample normal direction could be calculated using the relation $\theta_{EA} = \arctan\frac{M_{H=0,IP}}{M_{H=0,OOP}}$. The obtained results (at 20 K) are summarized in Figure 3b, which reveals a dramatically modified magnetic easy axis of SRO via exfoliation.

Bulk SRO with an orthorhombic structure processes a primary magnetocrystalline anisotropy with a magnetic easy axis along its orthorhombic $[010]_o$ direction.[30] For strained SRO thin films grown on LSAT, STO, and DSO substrates, the θ_{EA} angles were 6°, 21°, and 72°, respectively (Figure 3b) because of the different imposed epitaxial strains. Additionally, the magnetic hysteresis loops (M-H) (Figure S6a,b, Supporting Information) of the compressive-strained SRO films indicated that the magnetic easy axis was indeed close to the OOP direction, as evidenced by the square-like hysteresis loop along the OOP and smaller magnetizations along the IP. For all freestanding nanomembranes, the magnetic easy axis turned close to the in-plane direction ($\theta_{EA} \approx 76°$; Figure 3b). The magnetic anisotropy of freestanding membranes was dramatically different from that of compressively strained membranes, whereas it was close to that of the tensile-strained sample. This modified magnetic anisotropy was further supported by the smoothly curved magnetic hysteresis loops of the freestanding nanomembranes along both the OOP and IP directions (Figure S6, Supporting Information). Note that this modified magnetic anisotropy can be further correlated to epitaxial-strain-induced oxygen octahedral rotations (OOR),[26,31,32] which will be discussed later.

2.4. Electronic Transport Measurements

With knowledge of the ferromagnetic properties, we further probed the electronic transport properties of the freestanding

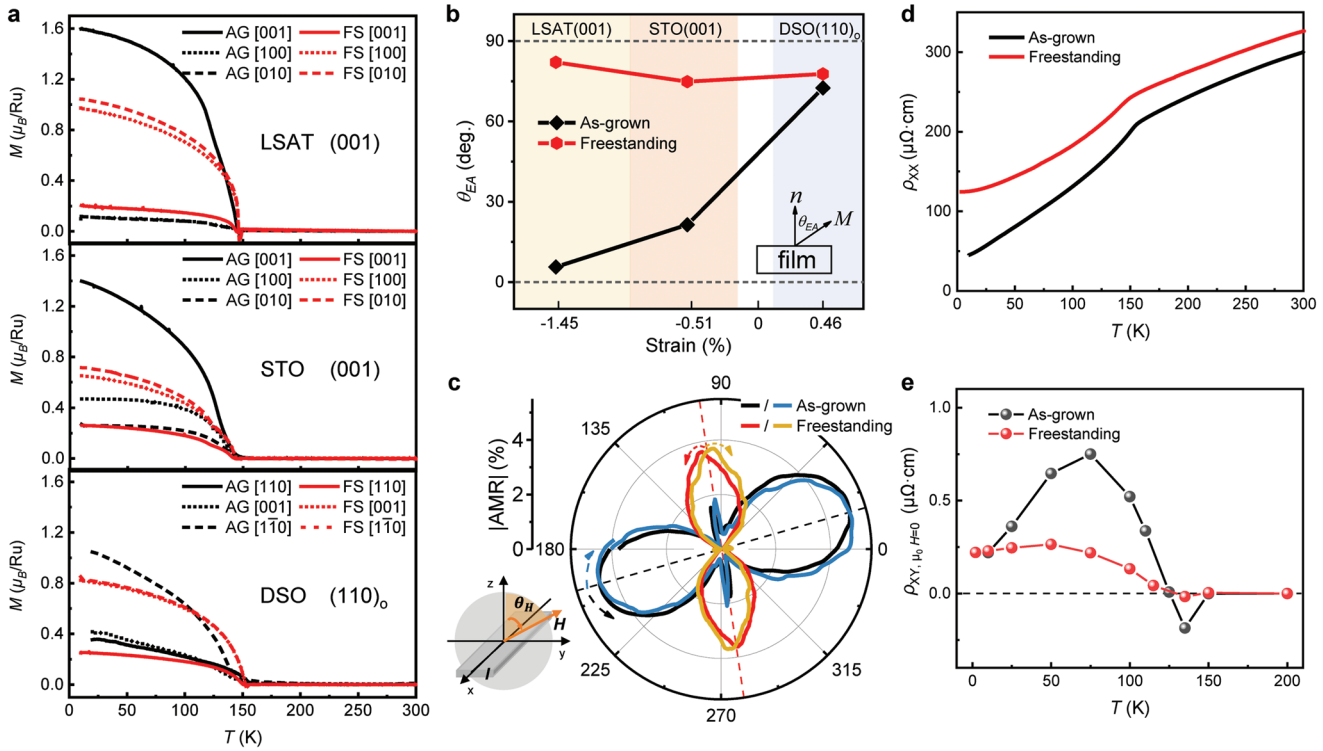

Figure 3. Modulated magnetic anisotropy for strained SRO $(001)_{pc}$ thin films and corresponding freestanding nanomembranes. a) Temperature-dependent remnant magnetization of strained SRO thin films (black) and freestanding nanomembranes transferred on silicon (red). b) Strain-dependent magnetic easy axis (θ_{EA}) for strained SRO films (black) and corresponding freestanding nanomembranes (red). Remnant magnetization at 20 K was used for the analysis. c) Angle-dependent magnetoresistance of strained SRO thin film on an STO (001) substrate (blue: clockwise, black: anticlockwise) and freestanding nanomembranes (orange: clockwise, red: anticlockwise). The temperature was 10 K, and the applied magnetic field was 8 T. The inset shows a schematic of the experimental configuration, in which the electrical current was applied along the *x*-axis, and the external magnetic field rotated within the *x*-plane. θ_H indicates the angle from the *z*-axis. d,e) Comparison of temperature-dependent longitudinal resistivity (ρ_{xx}, d) and anomalous Hall resistivity (ρ_{xy}, e) for strained thin films on STO (001) and their corresponding freestanding nanomembranes.

membranes, with epitaxially strained SRO/SCO/STO (001) as a reference. First, we performed angular-dependent magnetoresistance (AMR) measurement $\left(\frac{\Delta\rho}{\rho_0}=\frac{\rho(\theta_H)-\rho_0}{\rho_0}\right)$ (Figure 3c), in which the amplitude of the applied magnetic field was between the required saturated magnetic fields along the easy and hard axes. Therefore, the AMR results manifested a systematic evolution with a period of 180°, and the peak position corresponded to the magnetic easy axis. For strained SRO thin films on STO (001), the peaks were located at 16° (196°), indicating that the magnetic easy axis was close to the OOP. For the freestanding nanomembrane, the peaks shifted to 82° (262°), which was close to the IP. Furthermore, we observed a significant difference in magnetoresistance $\left(MR=\frac{\rho_{xx}(H)-\rho_{xx}(0)}{\rho_{xx}(0)}\right)$, where a larger negative MR signal was obtained along the easy axis (Figure S7a and S7b, Supporting Information).

The temperature-dependent longitudinal resistivity measurements ($\rho_{xx}(T)$, Figure 3d) revealed metallic behavior in both samples with a characteristic kink feature around T_c (≈150 K). Moreover, the magnetic field-dependent anomalous Hall resistivity (ρ_{xy}) measurements demonstrated similar square-like magnetic loops for both cases (Figure S7c,d, Supporting Information), while distinct hump features were clearly identified for the nanomembrane samples in the temperature range of 75—115 K. Although this feature exhibited great similarity with the previously reported topological Hall effect in ultrathin SRO with inequivalent interfaces,[33] the interface-driven Dzyaloshinskii–Moriya mechanism could be safely ruled out because the thick nanomembrane was free of any inequivalent interface/surface. Instead, we attributed this to the evolution of the Berry curvature[34] with the rotation of the magnetic axis, as revealed recently in tensile-strained SRO.[21] Figure 3e summarizes the anomalous Hall resistivity extracted at zero field for both the as-grown and nanomembrane samples, where a non-monotonic temperature dependence was observed in the as-grown sample, indicating the contribution of the Berry curvature.[34] For the freestanding sample, we observed a nearly monotonic dependence with a clearly suppressed magnitude of the Hall resistivity, which indicates a change in the Berry curvatures because the Weyl points might be located far from the Fermi energy.[21,34] For the freestanding membrane, the anomalous Hall resistivity approached zero at a temperature well below the Curie temperature. This result can be attributed to the modified magnetic anisotropy[21] through strain relaxation, in which the out-of-plane remnant magnetization was significantly smaller than the saturated value.

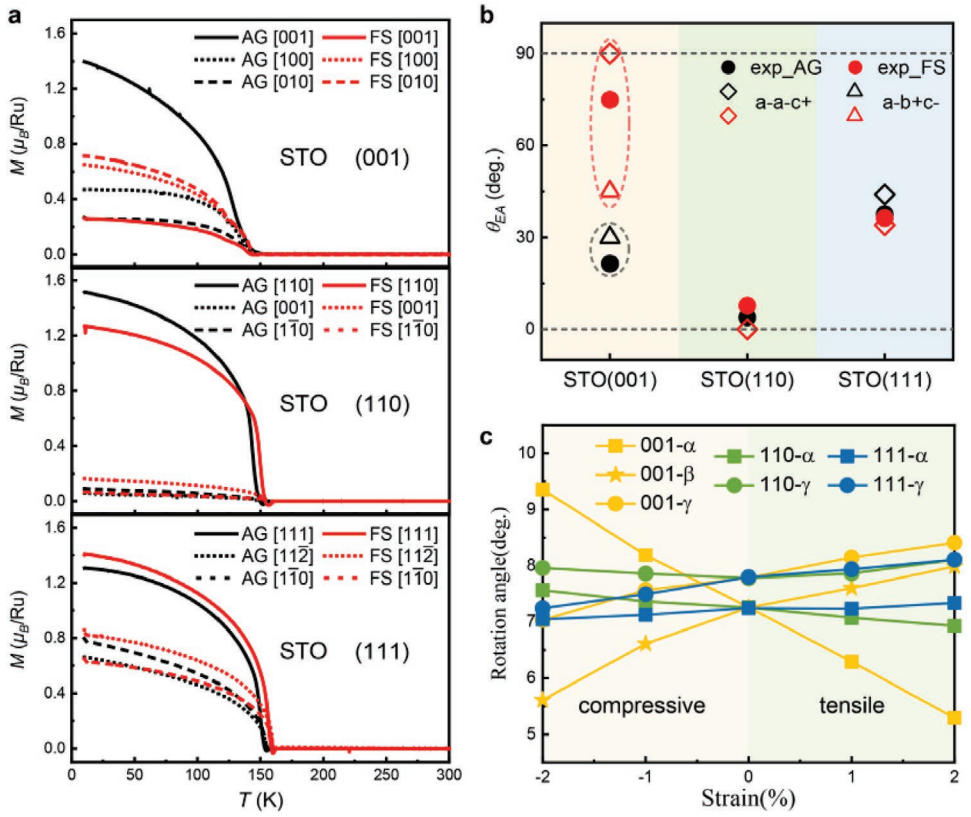

Figure 4. Evolution of magnetic anisotropy in SRO nanomembranes with different crystalline orientations. a) Temperature-dependent remnant magnetization for as-grown thin films (AG, black) and corresponding freestanding nanomembranes transferred onto silicon wafers (FS, red) measured along the pseudo-cubic [001], [110], and [111] directions. b) Comparison of experimentally observed and theoretically calculated magnetic easy axis (θ_{EA}) before and after exfoliation. The solid (hollow) symbols are the experimental (theoretical) results, in which the black and red symbols represent the as-grown thin films and freestanding nanomembranes, respectively. For the theoretical results, the diamond symbols represent *a–a–c+* oxygen octahedral rotation, whereas the triangle symbols represent *a–b+c–* oxygen octahedral rotation. c) Calculated strain-dependent oxygen octahedral rotation angles for $(001)_{pc}$- (yellow), $(110)_{pc}$- (green), and $(111)_{pc}$- (blue) oriented SRO films. For $(001)_{pc}$ orientation, we considered the *a–b+c–* oxygen octahedral rotation pattern, in which the square, star, and circle symbols represent the α, β, and γ rotation angles, respectively. For the $(110)_{pc}$ and $(111)_{pc}$ orientations, we considered *a–a–c+* oxygen octahedral rotation, in which the square symbols represent the α rotation angle ($\beta = \alpha$) and the circle symbols represent the γ rotation angle.

2.5. Crystalline Orientation-Dependent Freestanding Nanomembranes

Note that previous studies on freestanding oxide nanomembranes mainly focused on $(001)_{pc}$-oriented perovskite thin films owing to the limitation of the employed buffered layers. Because of the closely matched epitaxial relationship between the SCO and perovskite structures, we were able to extend the studies to various crystalline orientations. By selecting STO (110) and (111) substrates, we obtained high-quality epitaxially strained SRO and subsequent freestanding nanomembranes with different crystalline orientations (Figure S8, Supporting Information). Because of the relatively smaller lattice constant of cubic STO compared to SRO, all as-grown samples were compressively strained, whereas the strain was entirely relaxed for freestanding nanomembranes. With these samples, we further investigated the evolution of magnetic anisotropy between the strained and corresponding freestanding SRO membranes with various orientations. The magnetic easy axis, characterized by the tilting angle of θ_{EA}, was estimated through remnant (zero field) *M-T* measurements (**Figure 4**a), with the cooling magnetic field applied along three mutually perpendicular directions. For the SRO $(001)_{pc}$ case, we observed a change in the magnetic easy axis from close-OOP toward IP. Meanwhile, the SRO $(110)_{pc}$ and SRO $(111)_{pc}$ samples exhibited a robust easy axis (Figure 4b), which was further supported by typical *M-H* loop measurements (Figure S9, Supporting Information).

Owing to the strong spin-orbit coupling in SRO, we deduced that the different magnetic anisotropies for different oriented SRO were closely related to their distinct structural variants, especially the oxygen octahedral rotations (OOR).[26–28] Next, we combined first-principles calculations and high-resolution XRD measurements to elucidate this issue. While bulk SRO has an *a–a–c+* OOR pattern (using Glazer notation), experimentally, an *a–b+c–*/*a+b–c–* domain-mixed OOR pattern is observed in SRO thin films grown on STO (001) substrates.[10] Our first-principles calculations revealed that the magnetic easy axis tilting angle (θ_{EA}) was approximately 30° for strained SRO $(001)_{pc}$ with an *a–b+c–* OOR pattern, which was in reasonable agreement with the experimental value. For freestanding SRO $(001)_{pc}$ nanomembranes with an *a–b+c–* OOR pattern, the calculations indicated that θ_{EA} changed to 45°, whereas experimentally, θ_{EA}

was approximately 75° (Figure 4b). (Recalling the evolution of in-plane magnetic anisotropy, we speculated that this was related to the strain relaxation-induced OOR change.) Indeed, our high-resolution XRD measurements (Figure S10, Supporting Information) revealed that in addition to the *a*–*b*+*c*– OOR pattern, a bulk-like *a*–*a*–*c*+ OOR pattern could also be identified for the freestanding nanomembranes. With this knowledge, we further calculated the θ_{EA} angle for freestanding thin films with an *a*–*a*–*c*+ pattern, obtaining a value of 90°. Thus, the experimental magnetic tilting angle (θ_{EA}) could be understood as the average over these two OOR patterns. Unlike the $(001)_{pc}$ case, our calculations showed a tilting angle θ_{EA} similar to the experimental data for the other two oriented samples by considering only one bulk-like *a*–*a*–*c*+ OOR pattern. Specifically, for the SRO $(110)_{pc}$ samples, the calculated θ_{EA} was ≈0° for both the strained and freestanding samples, which was in good agreement with our experimental values (θ_{EA} < 10° for both cases). For the SRO $(111)_{pc}$ samples, our calculations revealed that the tilting angle θ_{EA} was 44°, which was close to the experimental value of 38°; furthermore, this changed to 35° for the freestanding sample, which was in excellent agreement with the experimental value of 36°.

To understand why multiple OOR patterns emerge in the SRO $(001)_{pc}$ freestanding membranes, we calculated the rotation angles (α, β, γ)[35] of different OOR patterns (Figure S11, Supporting Information) as a function of epitaxial strain for different crystalline orientations. We found that all three rotation angles (α, β, γ) exhibited pronounced changes with epitaxial strain for SRO $(001)_{pc}$, whereas the changes in rotation angles in the $(110)_{pc}$ and $(111)_{pc}$ samples were significantly smaller (Figure 4c). This result clearly suggests that, compared to the $(110)_{pc}$ and $(111)_{pc}$ films, more elastic energy was released in the $(001)_{pc}$ thin films during strain relaxation, providing a favorable condition for the switching of the OOR pattern.

3. Conclusion

In summary, we demonstrated that brownmillerite SCO is a promising sacrificial layer to manipulate freestanding oxide nanomembranes and obtained a series of high-quality and large-scale SRO nanomembranes from wide-range strained and various oriented substrates. Our results revealed a series of dramatic evolutions in the magnetic anisotropy of SRO through freestanding engineering, which forms a fertile ground for exploring the novel functionalities of SRO for flexible electronics. This study offers the possibility to explore flexible electronics from a wide range of complex oxides with different strained states and crystalline orientations, and we envision that these enriched material systems will lead to a wide spectrum of novel electronic states.

4. Experimental Section

Growth of SRO Heterostructures: Heterostructures of $SrRuO_3$/$SrCoO_{2.5}$, $SrCoO_{2.5}$ (SCO), and $SrRuO_3$ (SRO) thin films were grown on different substrates via pulsed laser deposition. The SCO layers were grown at a temperature of 750 °C under an oxygen partial pressure of 13 Pa with a laser (KrF, λ = 248 nm) energy density of 1.1 J cm^{-2} and a repetition rate of 2 Hz. The SRO layers were gown under an oxygen partial pressure of 13 Pa, substrate temperature of 700 °C, laser energy density of 2 J cm^{-2}, and repetition rate of 2 Hz. After deposition, the samples were cooled to 30 °C under growth pressure with a cooling rate of 7 °C min^{-1}. The sample thickness was controlled by the growth time at the calibrated growth rate and confirmed through X-ray reflectometry measurements.

Fabrication of SRO Freestanding Membranes: Approximately 0.5 mm thick PDMS was adhered to the surface of $SrRuO_3$ thin films (5 × 5 mm^2). Then, the heterostructure was immersed in vinegar, a carbonated drink, or 36% acetic acid solution at room temperature to dissolve the SCO sacrificed layer. When the SCO layer was completely dissolved in the solution, the freestanding nanomembrane that adhered to the PDMS support was removed from the solution and placed on a clean and polished silicon wafer (or other substrates). The flat surface of the silicon wafer was essential for achieving better physical absorption with the $SrRuO_3$ membrane. Subsequently, the PDMS support layer was gently pressed for close contact between the bottom surface of the $SrRuO_3$ membrane and silicon wafer. Next, the entire sample (including the silicon wafer, $SrRuO_3$ membrane, and PDMS support) was heated at 80 °C for 15 min, and this temperature was sufficiently low to avoid large deformation of PDMS. After heating, the PDMS support was readily detached. Finally, the high-crystalline-quality freestanding membrane with an intact size and atomically smooth morphology was successfully adhered to the silicon wafer. Etching and exfoliation were performed under ambient conditions.

Structural, Magnetization, and Transport Measurements: The crystalline structures of the as-grown thin films and freestanding nanomembranes were characterized using a high-resolution four-circle X-ray diffractometer (Smartlab, Rigaku) with monochromatic Cu $K_{\alpha 1}$ radiation (λ = 1.5406 Å). 2θ-ω scan and reciprocal space mapping (RSM) measurements were performed to determine both the out-of-plane and in-plane lattice constants before and after exfoliation. The magnetic properties of all samples, including temperature-dependent magnetization (M-T) and magnetic hysteresis loops (M-H), were measured using a 7 T Magnetic Property Measurement System (Quantum Design). For the remnant magnetization measurements, the sample was first field-cooled from 300 to 10 K under a magnetic field of 5 T, and then the magnetization was measured at zero field during warming. Electronic transport measurements were conducted in a standard Hall bar geometry with a 9 T PPMS DynaCool system (Quantum Design). The AMR was defined as $AMR = \frac{\rho(\theta_H) - \rho_0}{\rho_0}$, where $\rho(\theta_H)$ refers to the resistivity with the magnetic field applied along the θ_H direction, and ρ_0 denotes the maximum value of longitudinal resistivity.

Transmission Electron Microscopy Measurements: Cross-sectional transmission electron microscopy (TEM) specimens were prepared by thinning the sample to less than 30 µm via mechanical polishing, followed by argon ion milling in a Precision Ion Polishing System 691 (Gatan). For plan-view TEM characterization, a freestanding nanomembrane was attached to the lacey carbon film side of the holey Cu TEM grid. High-angle annular dark-field (HAADF) images and energy-dispersive X-ray spectroscopy (EDX) maps were obtained using an aberration-corrected FEI (Titan Cubed Themis G2) microscope operating at 300 kV.

High-Resolution Synchrotron X-ray Thin-Film Diffraction Measurements: For detailed OOR-induced half-order-peak investigations, high-resolution synchrotron X-ray thin-film diffraction measurements were conducted at the beamline sector 12-ID-D of the Advanced Photon Source at the Argonne National Laboratory. To minimize the fluorescence signal from the substrate, high-energy (E = 20 keV) X-rays were used. Geometric correction and background subtraction were employed for data analysis.

First-Principles Calculations: First-principles calculations were performed using the Vienna Ab Initio Simulation Package (VASP).[36,37] We used the generalized gradient approximation with Perdew–Burke–Ernzerhof parameterization (GGA-PBE) as the exchange-correlation functional.[38] We used an energy cutoff of 600 eV and 10 × 10 × 8 Monkhorst–Pack *k*-points to sample the Brillouin zone.[39] Spin-orbit coupling (SOC) was included in all calculations. We employed a bulk

$SrRuO_3$ crystallized in an orthorhombic crystalline structure symmetry (*Pnma*, space group No. 62). We first determined the pseudo-cubic lattice constants by fully relaxing the crystal structure of bulk $SrRuO_3$ until each force component was smaller than 0.01 eV $Å^{-1}$ and the pressure on the simulated cell was less than 0.5 kbar. It was found that the simulated lattice constant u_0 equaled 3.977 Å, which was in good agreement with the experimental pseudo-cubic lattice of 3.927 Å.[40] Then, we studied $SrRuO_3$ under bi-axis strain. We considered three different orientations of [001], [110], and [111], which were the growth directions (see Figure S11, Supporting Information). For all three orientations, the *a*–*a*–*c*+ oxygen octahedral rotation pattern was first studied. Additionally, we studied the *a*–*b*+*c*– oxygen octahedral rotation pattern for the [001] orientation. We imposed bi-axial strain by fixing the two in-plane lattice constants. The bi-axial strain is defined as $\delta = \frac{u-u_0}{u_0} \times 100\%$, where u is the lattice constant of the substrate. For instance, to simulate $SrRuO_3$ thin films grown on $SrTiO_3$ substrates, 0.5% compressive strain ($\delta = -0.5\%$) was applied to $SrRuO_3$. For a given strain, the out-of-plane lattice constant and all internal atomic coordinates were optimized.

Supporting Information

Supporting Information is available from the Wiley Online Library or from the author.

Acknowledgements

This study was financially supported by the National Key R&D Program of China (2021YFE0107900, 2021YFA1400300), Basic Science Center Program of NSFC (grant No. 51788104), NSFC (grant Nos. 51872155 and 52025024), Beijing Nature Science Foundation (grant no. Z200007), and Beijing Advanced Innovation Center for Future Chip (ICFC). N.L. acknowledges the support of the NSFC (grant No. 11974401), the Strategic Priority Research Program of the Chinese Academy of Sciences (No. XDB33000000). H.C. acknowledges the support of the NSFC (grant No. 11774236). This research used the resources of the Advanced Photon Source, a U.S. Department of Energy (DOE) Office of Science User Facility, operated for the DOE Office of Science by Argonne National Laboratory under Contract No. DE-AC02-06CH11357. Extraordinary facility operations were supported in part by the DOE Office of Science through the National Virtual Biotechnology Laboratory, a consortium of DOE national laboratories that focused on the response to COVID-19, with funding provided by the Coronavirus CARES Act. Figure 3 and S7 were corrected and instances of ρ_{yx} in the main manuscript were corrected as ρ_{xy} on July 11, 2022 after initial online publication.

Conflict of Interest

The authors declare no conflict of interest.

Data Availability Statement

The data that support the findings of this study are available from the corresponding author upon reasonable request.

Keywords

brownmillerite, freestanding thin films, magnetic anisotropy, sacrificial layers, $SrCoO_{2.5}$, $SrRuO_3$

Received: November 22, 2021
Revised: March 25, 2022
Published online: April 12, 2022

[1] H. Y. Hwang, Y. Iwasa, M. Kawasaki, B. Keimer, N. Nagaosa, Y. Tokura, *Nat. Mater.* **2012**, *11*, 103.
[2] R. Ramesh, N. A. Spaldin, *Nat. Mater.* **2007**, *6*, 21.
[3] D. Khomskii, *Transition metal compounds*, Cambridge University Press, Cambridge, United Kingdom **2014**.
[4] J. Ngai, F. Walker, C. Ahn, *Annu. Rev. Mater. Res.* **2014**, *44*, 1.
[5] D. Lu, D. J. Baek, S. S. Hong, L. F. Kourkoutis, Y. Hikita, H. Y. Hwang, *Nat. Mater.* **2016**, *15*, 1255.
[6] D. Ji, S. Cai, T. R. Paudel, H. Sun, C. Zhang, L. Han, Y. Wei, Y. Zang, M. Gu, Y. Zhang, *Nature* **2019**, *570*, 87.
[7] G. Dong, S. Li, M. Yao, Z. Zhou, Y. Zhang, X. Han, Z. Luo, J. Yao, B. Peng, Z. Hu, *Science* **2019**, *366*, 475.
[8] S. S. Hong, M. Gu, M. Verma, V. Harbola, H. Y. Hwang, *Science* **2020**, *368*, 71.
[9] Q. Gan, R. A. Rao, C. Eom, J. L. Garrett, M. Lee, *Appl. Phys. Lett.* **1998**, *72*, 978.
[10] W. Lu, P. Yang, W. D. Song, G. M. Chow, J. S. Chen, *Phys. Rev. B* **2013**, *88*, 214115.
[11] W. M. Lu, W. Song, P. Yang, J. Ding, G. M. Chow, J. S. Chen, *Sci. Rep.* **2015**, *5*, 10245.
[12] D. M. Paskiewicz, R. Sichel-Tissot, E. Karapetrova, L. Stan, D. D. Fong, *Nano Lett.* **2016**, *16*, 534.
[13] S. R. Bakaul, C. Serrao, M. Lee, C. W. Yeung, A. Sarker, S. Hsu, A. K. Yadav, L. R. Dedon, L. You, A. I. Khan, *Nat. Commun.* **2016**, *7*, 10547.
[14] Y. Zhang, L. Shen, M. Liu, X. Li, X. Lu, L. Lu, C. Ma, C. You, A. Chen, C. Huang, *ACS Nano* **2017**, *11*, 8002.
[15] R. Guo, L. You, W. Lin, A. Abdelsamie, J. Chen, *Nat. Commun.* **2020**, *11*, 2571.
[16] Z. Chen, B. Y. Wang, B. H. Goodge, D. Lu, S. S. Hong, D. Li, L. F. Kourkoutis, Y. Hikita, H. Y. Hwang, *Phys. Rev. Mater.* **2019**, *3*, 060801.
[17] R. Xu, J. Huang, E. S. Barnard, S. S. Hong, P. Singh, E. K. Wong, T. Jansen, V. Harbola, J. Xiao, B. Y. Wang, *Nat. Commun.* **2020**, *11*, 3141.
[18] D. Li, C. Adamo, B. Y. Wang, H. Yoon, Z. Chen, S. S. Hong, D. Lu, Y. Cui, Y. Hikita, H. Y. Hwang, *Nano Lett.* **2021**, *21*, 4454.
[19] Z. Lu, J. Liu, J. Feng, X. Zheng, L.-h. Yang, C. Ge, K.-j. Jin, Z. Wang, R.-W. Li, *APL Mater.* **2020**, *8*, 051105.
[20] P. T. Le, E. Johan, G. Koster, *Sci. Rep.* **2021**, *11*, 12435.
[21] D. Tian, Z. Liu, S. Shen, Z. Li, Y. Zhou, H. Liu, H. Chen, P. Yu, *Proc. Natl. Acad. Sci. U.S.A.* **2021**, *118*, e2101946118.
[22] H. Kum, H. Lee, S. Kim, S. Lindemann, W. Kong, K. Qiao, P. Chen, J. Irwin, J. H. Lee, S. Xie, *Nature* **2020**, *578*, 75.
[23] A. Muñoz, C. de la Calle, J. Alonso, P. M. Botta, V. Pardo, D. Baldomir, J. Rivas, *Phys. Rev. B* **2008**, *78*, 054404.
[24] N. Lu, P. Zhang, Q. Zhang, R. Qiao, Q. He, H. B. Li, Y. Wang, J. Guo, D. Zhang, Z. Duan, *Nature* **2017**, *546*, 124.
[25] G. Koster, L. Klein, W. Siemons, G. Rijnders, J. S. Dodge, C.-B. Eom, D. H. Blank, M. R. Beasley, *Rev. Mod. Phys.* **2012**, *84*, 253.
[26] D. Kan, R. Aso, R. Sato, M. Haruta, H. Kurata, Y. Shimakawa, *Nat. Mater.* **2016**, *15*, 432.
[27] Z. Cui, A. J. Grutter, H. Zhou, H. Cao, Y. Dong, D. A. Gilbert, J. Wang, Y.-S. Liu, J. Ma, Z. Hu, *Sci. Adv.* **2020**, *6*, eaay0114.
[28] J. Zhou, X. Shu, W. Lin, D. F. Shao, S. Chen, L. Liu, P. Yang, E. Y. Tsymbal, J. Chen, *Adv. Mater.* **2021**, 2007114.
[29] L. Klein, J. Dodge, C. Ahn, J. Reiner, L. Mieville, T. Geballe, M. Beasley, A. Kapitulnik, *J. Phys.: Condens. Matt.* **1996**, *8*, 10111.
[30] A. Marshall, L. Klein, J. Dodge, C. Ahn, J. Reiner, L. Mieville, L. Antagonazza, A. Kapitulnik, T. Geballe, M. Beasley, *J. Appl. Phys.* **1999**, *85*, 4131.
[31] Q. Qin, W. Song, S. He, P. Yang, J. S. Chen, *J. Phys. D: Appl. Phys.* **2017**, *50*, 215002.
[32] L. Liu, Q. Qin, W. Lin, C. Li, Q. Xie, S. He, X. Shu, C. Zhou, Z. Lim, J. Yu, *Nat. Nanotech.* **2019**, *14*, 939.

[33] J. Matsuno, N. Ogawa, K. Yasuda, F. Kagawa, W. Koshibae, N. Nagaosa, Y. Tokura, M. Kawasaki, *Sci. Adv.* **2016**, *2*, e1600304.
[34] Z. Fang, N. Nagaosa, K. S. Takahashi, A. Asamitsu, R. Mathieu, T. Ogasawara, H. Yamada, M. Kawasaki, Y. Tokura, K. Terakura, *Science* **2003**, *302*, 92.
[35] S. May, C. Smith, J.-W. Kim, E. Karapetrova, A. Bhattacharya, P. Ryan, *Phys. Rev. B* **2011**, *83*, 153411.
[36] G. Kresse, J. Hafner, *Phys. Rev. B* **1994**, *49*, 14251.
[37] G. Kresse, J. Furthmüller, *Phys. Rev. B* **1996**, *54*, 11169.
[38] J. P. Perdew, K. Burke, M. Ernzerhof, *Phys. Rev. Lett.* **1996**, *77*, 3865.
[39] H. J. Monkhorst, J. D. Pack, *Phys. Rev. B* **1976**, *13*, 5188.
[40] T. Kiyama, K. Yoshimura, K. Kosuge, Y. Ikeda, Y. Bando, *Phys. Rev. B* **1996**, *54*, R756.